Influence of Thermal Diffusion on the Spatial Resolution in Photothermal Microscopy

Brendan S. Brown and Gregory V. Hartland*

Department of Chemistry and Biochemistry, University of Notre Dame, Notre Dame,

IN 46556, USA

Abstract: In photothermal heterodyne imaging (PHI) experiments a time-modulated pump beam

heats the sample, creating a thermal lens that is detected by non-resonant probe. This technique is

very sensitive, and has been used to study a variety of systems. The extent of heat diffusion in the

system depends on the timescale for the experiment, which is determined by the pump beam

modulation frequency. In this paper the way the spatial resolution in PHI microscopy changes

with modulation frequency was studied through experiments and heat transfer simulations on gold

nanoparticles. The experiments were performed with both focused and widefield pump beams.

For a focused pump beam, changing modulation frequency had no effect on the spatial resolution.

A small frequency effect was observed for a widefield pump, but the magnitude was much less

than that expected from the thermal diffusion lengths in the system. The simulations also showed

a small frequency dependence for the spatial extent of heating, consistent with the measurements.

This arises because the system rapidly reaches a steady-state condition in these experiments, where

the rate of optically heating the particle matches the rate of heat dissipation. In this limit the

temperature profile around the particle simply decays inversely with distance, and is independent

of the thermal diffusion length.

* Corresponding Author: e-mail ghartlan@nd.edu

1

1. Introduction:

Photothermal heterodyne imaging (PHI) is a widely used technique for imaging and spectroscopic studies of nanomaterials. ¹⁻⁷ It is capable of detecting small metal and semiconductor nanoparticles, ^{2,8-11} and even single molecules. ¹² It has also been used to study biological samples and soft materials, ¹³⁻¹⁷ and for super resolution infrared imaging (IR-PHI). ¹⁸⁻²¹ In PHI a modulated pump beam is used to heat the sample through absorption. The heat dissipates into the surrounding medium, which causes a temperature, and thus refractive index gradient. ^{7,22-28} The refractive index gradient, also known as a thermal lens, is probed by a second non-resonant probe laser beam. The thermal lens changes the transmission or reflection of the probe beam, creating the PHI signal. ^{7,22-28} In these experiments the characteristic length scale for heat diffusion into the medium is given by the thermal radius $R_{th} = \sqrt{2\kappa/\omega C}$, where κ is the thermal conductivity of the medium, C is the volume-specific heat capacity and ω is the pump beam modulation frequency. ^{1,23,29-30} The ω dependence of R_{th} raises the question of whether the spatial resolution in PHI measurements depends on the modulation frequency.

Traditionally PHI experiments are performed at modulation frequencies above several hundred kHz, even though the PHI signal is maximized at low frequencies.^{22,31-33} This is to reduce the 1/f noise and, thus, enhance sensitivity.²²⁻²³ At high frequencies the thermal diffusion length is very short, much less than the diffraction limit for the laser beams. Frequencies lower than 50 kHz have not been extensively studied due to the aforementioned 1/f noise issues. Although at these frequencies the thermal diffusion lengths become larger than the point spread function of the laser beams in a typical microscope experiment, making this an interesting region to study. IR-PHI experiments are also sometimes implemented at low modulation frequencies due to limitations in the laser sources.¹⁸⁻²¹ Several previous studies have investigated how the phase of the PHI signal

changes with modulation frequency,³²⁻³⁵ providing information about the thermal diffusivity of the surroundings,³³⁻³⁵ as well as a way to improve contrast in measurements of complex samples.³² However, the way the timescale for the PHI experiments, and the associated thermal diffusion lengths, affect the spatial resolution in PHI has not been investigated in detail.

In this study the frequency dependence of the spatial resolution in PHI was examined through both experiments and finite element simulations of heat diffusion. PHI images of gold nanoparticles on a glass surface in glycerol were recorded at different pump beam modulation frequencies using both co-focused pump and probe beams, and a widefield pump with a focused probe. The modulation frequency was varied from 500 kHz to 1 kHz, corresponding to thermal diffusion lengths ranging from $0.26~\mu m$ to $5.9~\mu m$ in glycerol.^{23,30} However, only slight changes in the spatial resolution in the images were observed. Finite element simulations of thermal transport confirm the experimental observations. Analysis of the simulations show that the small changes in the spatial resolution arise because the laser excited gold nanoparticles rapidly reach a steady-state condition, where the rate of heating is balanced by the rate of heat dissipation.³⁶ Under these conditions the temperature profile around the particles has a 1/r dependence, 28-30,33-34,36-40 and is independent of the modulation frequency and the associated thermal diffusion length.

2. Methods:

The experiments were performed on a homebuilt PHI microscope. A schematic diagram of the instrument is presented in the Supporting Information. An acousto-optic modulator (AOM, Intra-Action AOM-402AF1) was used to modulate the pump laser, which was a 532 nm wavelength beam produced by a Spectra-Physics Millenia Vs. The probe laser was a 636 nm Coherent Obis. A lock-in amplifier generated a square wave driving signal for the AOM, and

recorded the PHI signal. A Stanford Research Systems SR830 lock-in was used for the low frequency experiments, and a SR844 lock-in was used for frequencies above 100 kHz. The lockin time constant for the measurements varied between 10 ms and 300 ms, depending on the modulation frequency (higher time constants were needed for low modulation frequencies because of the increased 1/f noise), and whether the measurements were performed with a widefield or focused pump beam. Both the pump and probe were spatially filtered to improve the beam quality. The two beams were made collinear using a dichroic mirror (Thorlabs, DMLP567) and focused at the sample by a Nikon Plan Apo 40x/0.95 NA air objective. The experiments were performed in transmission mode using an Olympus UPlanFL 10x/0.30 NA air objective to recollimate the probe beam, and a Thorlabs PDA36A amplified photodetector (10x gain setting) to detect the probe power. The instrument was switched from focused to widefield pump by inserting a 250 mm focal length lens into the pump beam path before the dichroic mirror. The spot size of the pump beam in the widefield experiments was approximately 80 µm. The power density of the probe beam at the sample was ~12 MW/cm². The pump beam had a power density of 1.3 MW/cm² for the cofocused experiments, and 1.3 kW/cm² for the widefield experiments.

The PHI experiments were performed on 50 nm gold nanoparticles purchased from nanoComposix (product number AUCN50). Samples for microscopy experiments were prepared by drop casting 200 μ L of the stock solution onto a plasma cleaned BK7 #1.5 glass coverslip, and allowing the solution to rest for 10 minutes. After this time the excess liquid was removed by wicking with a paper towel. A drop of glycerol was added to the sample, and a 2nd plasma cleaned coverslip was placed on top to ensure a uniform optical environment for the measurements.

Finite Element (FE) simulations of heat transfer and diffusion for gold nanoparticles in different environments were performed using COMSOL Multiphysics (v5.3). Spherical gold

nanoparticles with diameters of either 20 nm or 50 nm were placed at the center of a larger sphere (typically 4 μm radius) that represents the surrounding medium. The size of the simulation domain was adjusted to ensure that the temperature profiles were not affected by the simulation boundaries. The simulations were performed using the Heat Transfer Module with the Time Dependent Solver in COMSOL. The boundary conditions for the simulations were constant temperature (300 K) for the exterior surface of the large sphere, and continuity of temperature at the different internal interfaces. The thermal conductivities, heat capacities and densities for the different materials in the simulations were either taken from COMSOL's library of materials, or from the data in Ref. [23]. The values used in the simulations are given in the Supporting Information. Simulations were performed for particles in a homogeneous environment, and for particles supported on a glass surface. The surrounding materials examined in the homogeneous medium simulations were glycerol, polymethylmethacrylate (PMMA), water and chloroform. For the glass supported particles, simulations were performed for glycerol and air environments. Note that we did not consider the effect of surface roughness in this work.⁴¹

Two different calculations were performed. In the majority of the simulations the gold nanoparticle was defined as a time-dependent heat source. The heat source was modelled as either a step function, or a 50% duty cycle square wave to match the output of the AOM. The power of the heat source was set to $P_0 = 1 \times 10^{-6}$ W, which gives a temperature rise of 11.3 K for the 50 nm particles in glycerol at the steady-state condition. For the 20 nm gold particles the power was scaled to account for the different volume of the particles. In these simulations the initial temperature of the gold was set to be the same as the environment (300 K). Simulations were also performed for the gold nanoparticles with an initial temperature of 310 K to examine the timescale for heat dissipation (shown in the Supporting Information). Temperature versus time plots were

created using point evaluation at the center of the gold particle, and line profiles of the temperature over the simulation domain were also extracted from the simulation results.

Note that we have not attempted to model the interaction of the probe beam with the thermal lens, $^{22, 24-28, 30, 42-44}$ as we are primarily interested in the spatial extent of thermal diffusion. For particles in a homogeneous environment we simply plot the temperature profiles around the particle to evaluate the size of the thermal lens. For the particles on glass surface, the temperature changes were multiplied by dn/dT for the different materials, see the Supporting Information for details.

3. Results and Discussion:

Figure 1 shows PHI images of 50 nm gold particles in glycerol recorded using co-focused pump and probe beams with different pump beam modulation frequencies (1 kHz, 10 kHz and 100 kHz). The thermal diffusion length in glycerol varies from 0.59 μm for a 100 kHz modulation frequency, to 5.9 μm at 1 kHz. Thus, if the spatial resolution in the experiments followed thermal diffusion, the images from the different particles in Figure 1 should be smeared together at low frequencies. However, the spatial resolution in Figure 1 clearly does not change with modulation frequency. Line profiles from the images recorded at high resolution (left side of Figure 1) show that the full-width-at-half-maximum (FWHM) varies by less than 0.1 μm for the different experiments. This result has a simple explanation: for co-focused pump and probe beams, heating only occurs when the pump beam is on the particle. ^{22, 24-28, 30, 42-44} If the pump is off the particle, there is no heating and no thermal lens. Thus, the spatial resolution in the PHI experiments is determined by the point spread function of the pump and probe beams, and not from the dimensions of the thermal lens. This also means that PHI experiments with co-focused pump and

probe beams image the nanoparticle absorption, and not the thermal lens generated by the heated nano-objects. 24-28, 30, 42-44

The situation is potentially different for a widefield pump beam, where the particle is continuously excited as the image is created. In this case a thermal lens is always present, and the probe beam can, in principle, image the extent of the thermal lens. Figure 2 shows examples of PHI images recorded at different modulation frequencies when the pump beam is much larger than

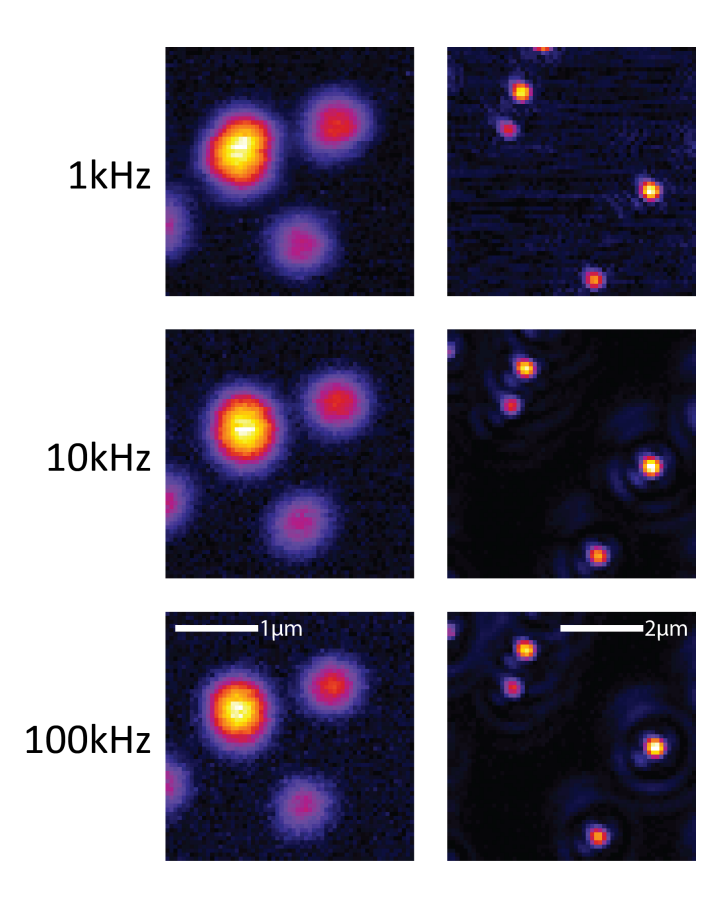


Figure 1: PHI images of 50 nm gold nanoparticles recorded with co-focused pump and probe beams. Left: $3x3~\mu m$ images recorded with a step size of $0.05~\mu m$. Right: $6x6~\mu m$ images recorded with a step size of $0.1~\mu m$. The pump beam modulation frequency is given in the figure. The lock-in time constant was 10 ms for the 10 kHz and 100 kHz experiments, and 100 ms for the 1 kHz experiment.

the probe beam. Note that the pump power density at the sample is significantly smaller for the widefield pump experiments compared to the focused pump experiments. This causes a lower signal level and, thus, a longer lock-in time constant is needed to achieve reasonable signal-to-noise. The spatial resolution in the widefield images is also about a factor of two worse than that in the focused pump images, presumably because the PHI point spread function is now determined by the longer wavelength probe laser. There are two important points to note from the images in Figure 2. First, there is a noticeable broadening of the features in the images as the frequency decreases. This indicates that the widefield pump images report on the thermal lens created around the particle. However, the sizes of features in the images are still much smaller than that expected from the thermal diffusion length at low frequencies. At 10 kHz the thermal radius in glycerol is $1.8 \mu m$ implying a FWHM greater than 3 μm , which is much larger than that in the experimental images.

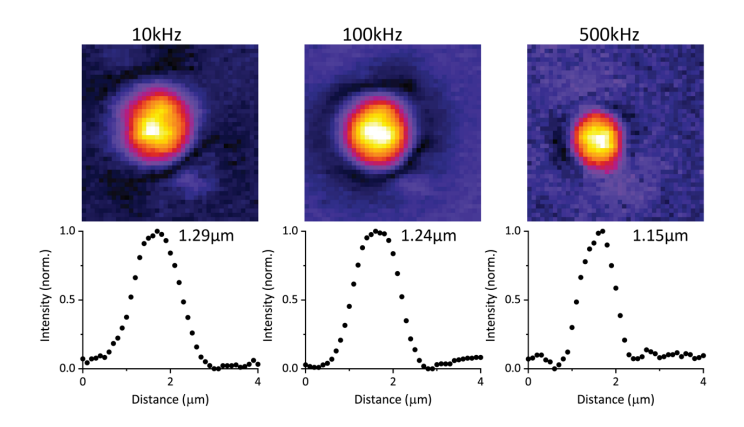


Figure 2: Top) PHI images recorded with a widefield pump beam at different modulation frequencies (4x4 μm image size, 0.1 μm step sizes with a lock-in time constant of 300 ms). Bottom) Corresponding line profiles (after background subtraction) taken by averaging along the x and y directions through the center of the particle. The FWHM determined from the profiles are given in the panels.

In order to understand the broadening (or lack of broadening) of the PHI signal with decreasing modulation frequency, FE simulations were performed to analyze heat dissipation in the system. We first examine particles in a homogeneous environment. In this case the spatial extent of the thermal lens in the system simply follows the temperature profile. Figure 3 shows simulated temperature profiles around 20 nm and 50 nm diameter gold particles in glycerol for a step function heating source. The different lines correspond to times of $0.01~\mu s$, $0.02~\mu s$, $0.05~\mu s$, $0.2~\mu s$, $5~\mu s$ and $50~\mu s$ after the heating has been turned on. The simulations show that the system reaches a steady-state condition very quickly, within a few tens of μs . Steady-state occurs when the rate of heating the particle matches the rate of heat dissipation in the environment. Once the system is at steady-state the temperature versus distance profiles are constant with time.

The problem of heat dissipation for a sphere in a homogeneous medium can be solved analytically. In particular, a fairly simple solution is obtained for constant heating of a spherical surface:³⁶

$$\Delta T(r,t) = \frac{Q}{8\pi\kappa ra} \left[\sqrt{\frac{4\Lambda t}{\pi}} \left(e^{-(r-a)^2/4\Lambda t} - e^{-(r+a)^2/4\Lambda t} \right) - |r - a| \operatorname{Erfc} \left(\frac{|r - a|}{\sqrt{4\Lambda t}} \right) \right]$$

$$+ (r + a) \operatorname{Erfc} \left(\frac{(r + a)}{\sqrt{4\Lambda t}} \right)$$

$$(1)$$

where $\Lambda = \kappa/\rho C_p$ is the thermal diffusivity of the medium, Q is the heating rate, and a is the particle radius. The results from Equation (1) are shown as the blacked dashed lines in Figure 3. The time dependent spatial profiles predicted by the analytic and FE calculations are in very good

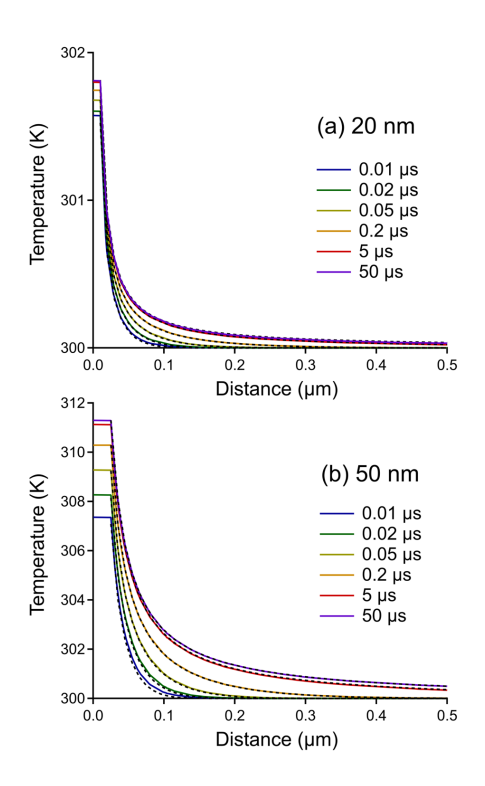


Figure 3: Temperature versus distance profiles for (a) 20 nm and (b) 50 nm particles calculated by FE simulations for a step function heating pulse. The different colored lines correspond to times of $0.01~\mu s$, $0.02~\mu s$, $0.05~\mu s$, $0.2~\mu s$, $5~\mu s$ and $50~\mu s$ after the start of heating. The dashed black lines show the temperature profiles calculated using Equation (1).

agreement, with slight differences at short times. These differences could arise because Equation (1) was derived for heat diffusion from a shell in a system where the thermal diffusivity is the same everywhere, which does not quite match the situation considered in the FE simulations. There could also be an issue with the accuracy of the FE solver for times just after the heating pulse has been turned on. At long times $(t \gg a^2/\kappa)$ Equation (1) reduces to the steady-state result of $\Delta T = Q/4\pi\kappa r$ for r > a.³⁶ Comparison of the FE simulations or the analytic results from Equation (1)

to 1/r curves shows that the temperature profiles are essentially identical to the steady state result after ca. 5 μ s for the 20 nm particles, and ca. 50 μ s for the 50 nm particles.

Note that the maximum temperature reached for the 20 nm particles in the simulations is less than that for the 50 nm particles. This is due to the faster heat dissipation rate for smaller particles compared to large particles, 45-46 which means that for an equivalent heating rate the temperature at steady-state is less for the smaller particles. Simulations of temperature decay for 20 nm and 50 nm particles for an initial temperature of 310 K are presented in the Supporting Information. The timescale for the decay is much faster for the 20 nm particles, and also decreases as the thermal conductivity of the environment increases.

The simulations presented in Figure 3 show that the temperature profile around the particle evolves in time, reaching steady-state on a time scale that depends on the size of the particle and the thermal properties of the environment. Because the thermal lens in the PHI experiments follows the temperature profile, in principle, differences in the spatial extent of the thermal lens could occur for different modulation frequencies. To investigate this effect, simulations were performed with a square wave heating source with different frequencies. The results are presented in Figure 4 for gold nanoparticles in glycerol. Figure 4(a) shows the temperature in the particle versus normalized time (time/period) for 20 nm and 50 nm particles at 10 kHz and 1 MHz modulation frequencies. At the higher frequency the heating versus time traces do not follow a square wave. This is due to the finite timescale for reaching steady-state conditions: at high frequencies the particle cannot reach the steady-state temperature or return to the initial state during the heating cycles. This effect is reduced for the smaller particles because of the faster heat dissipation times (see the Supporting Information).

To characterize the effect of changing frequency on the spatial extent of the PHI signal, average temperature versus distance profiles were determined from the time-dependent simulations (this was done by simply averaging the profiles over three periods). The averaged profiles for $10 \, \text{kHz}$ and $1 \, \text{MHz}$ modulation frequencies are shown in Figure 4 (b). The temperature versus distance profiles at low frequency are essentially identical to the 1/r steady-state profile.

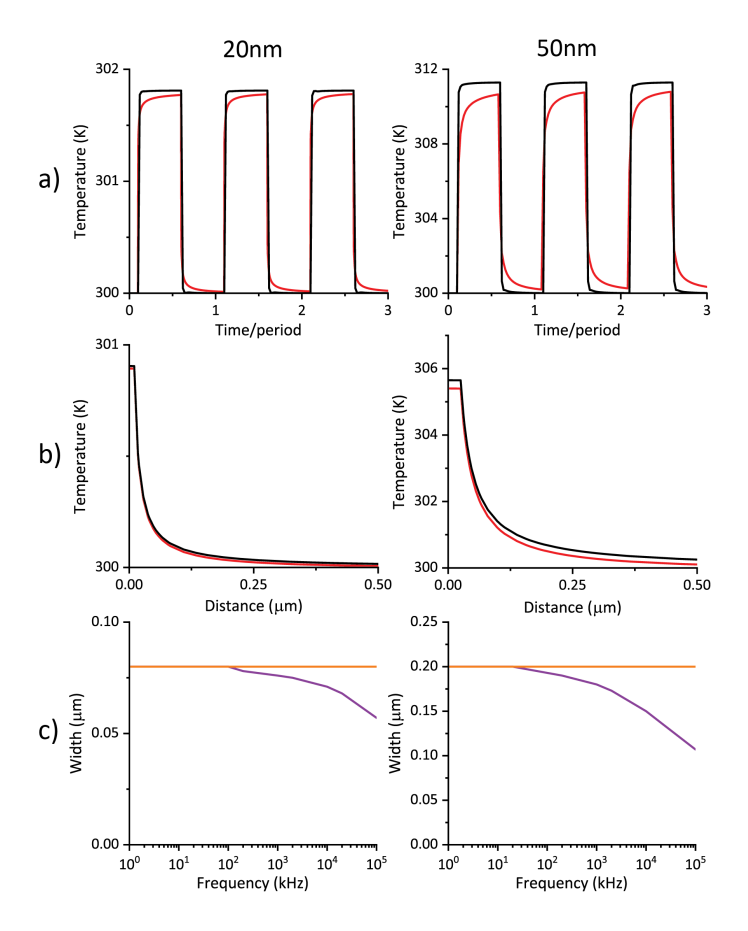


Figure 4: Simulation results for a square wave heat source with modulation frequencies of 10 kHz (black) and 1 MHz (red) for 20 nm (left) and 50 nm (right) diameter gold nanoparticles in glycerol. a) Temperature versus time/period. b) Temperature versus distance profiles averaged over three periods of heating. c) Full-width-at-quarter-maximum (FWQM) of the temperature profile (25% of ΔT_{max}). The horizontal orange lines show the FWQM values at steady state.

However, there are slight differences between the steady-state and simulation profiles at high frequencies. Interestingly, the frequency effects in the temperature versus distance profiles are small, even though the temperature versus time traces for the 50 nm particles in Figure 4(a) show significant differences for the two modulation frequencies.

The spatial extent of the temperature profile was characterized as the distance where the temperature falls to 25% of the maximum temperature in the temperature versus distance profiles, that is, where $\Delta T(r) = \Delta T_{particle}/4$. 25% of the maximum was chosen rather than the conventional 50% of the maximum to give numbers that are more commensurate with the experimental values, and because it represents a signal level that could be easily measured in a microscope experiment. The full-width-at-quarter-maximum (FWQM) values are plotted versus modulation frequency for 20 nm and 50 nm gold particles in glycerol in Figure 4(c). The orange horizontal lines show calculated FWQM values at the steady-state limit (for $\Delta T(r) \propto 1/r$, $\Delta T(r) = \Delta T_{particle}/4$ when $r = 4 \times$ the particle radius). The results show that the width of the temperature profile is essentially the same as the steady-state result for frequencies below 100 kHz for the 20 nm particles, and below 20 kHz for the 50 nm particles (consistent with the results in Figure 3). Overall the simulations in Figures 3 and 4 predict that there should only be small increases in the size of the features in the PHI images as the modulation frequencies is reduced, in agreement with the experimental results presented in Figure 2.

The effect of environment on the temperature profiles was also investigated. It has been shown that the choice of environment effects the signal-to-noise ratio for PHI, and there has been significant effort to find materials that produce larger PHI signals.^{23, 47-49} Figure 5 shows temperature versus time traces for 50 nm gold particles in water, glycerol, PMMA and chloroform, and averaged temperature versus distance profiles for two different modulation frequencies. As

noted above, at 1 MHz modulation frequency the system does not have enough time to reach the steady-state condition: there are noticeable rise and decay times in the temperature versus time traces, especially for chloroform. The simulations show that the maximum temperatures are in the order $\Delta T_{\rm CHCl_3} > \Delta T_{\rm PMMA} > \Delta T_{\rm glycerol} > \Delta T_{\rm H_2O}$. This does not follow the heat capacities of the materials. The heat capacity of chloroform is slightly larger than that of PMMA, yet the temperature change in chloroform is 60% larger. We interpret this observation as an effect from thermal conduction in the environment. At steady-state the temperature in the gold particle is determined by a balance between power in and heat diffusion away from the particle, which is controlled by the thermal conductivity of the environment.³⁶ From the expression for $\Delta T(r)$ given above, at steady-state $\Delta T_{particle} = Q/4\pi\kappa a$. Thus, environments with lower thermal

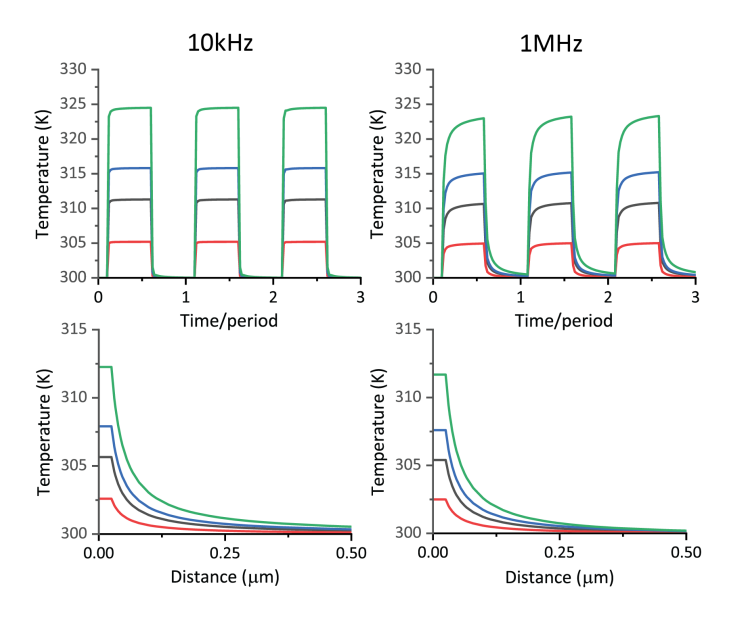


Figure 5: Simulation results for a 50 nm gold nanoparticle in 4 different environments for a square wave source with a 10 kHz or 1 MHz modulation frequency. Top) Temperature versus time for the gold nanoparticle and bottom) corresponding average temperature versus distance profiles (averaged over 3 periods). Red is water, black is glycerol, blue is PMMA and green is chloroform.

conductivities will create higher temperatures (more heat stored in the particles). The thermal conductivities for the different materials in the simulations are in the order $\kappa_{\text{CHCl}_3} < \kappa_{\text{PMMA}} < \kappa_{\text{glycerol}} < \kappa_{\text{H}_2\text{O}}$, leading to higher temperatures rises for chloroform compared to PMMA, PMMA compared to glycerol, and glycerol compared to water.

Note that the temperature versus distance profiles for the 10 kHz modulation frequency in Figure 5 are essentially equivalent for the different environments – apart from the different maximum temperatures. This is again because the system reaches the steady-state conditions at this modulation frequency, so the spatial profiles all fall off as 1/r. At 1 MHz modulation frequency there are slight differences in the temperature versus distance profiles, similar to the results presented in Figure 4.

Simulations were also performed for gold nanoparticles on a glass surface in glycerol and air environments. Note that for an inhomogeneous environment, we now have to include the temperature dependence of the refractive index to visualize the thermal lens. Figure 6 shows the temperature profiles and refractive index changes at steady-state for a gold particle with different amounts of embedding into the glass (100% embedding corresponds to the particle completely in glass with the top just touching the interface, and 0% corresponds to the particle completely in air/glycerol with the bottom touching the interface, see the Supporting Information for details). Temperature profiles through the center of the particle along lines perpendicular and parallel to the interface are shown in Figure 6(a) and 6(b), respectively. For Figure 6(a) glass is at negative distances and the different lines correspond to embeddings, from smallest to largest temperature change, of 100%, 75%, 50%, 25%, 10%, 5% and 0%. The data in Figure 6(b) corresponds to a 10% embedded particle. The temperature changes are smallest when the particles are completely embedded in glass, because of the higher thermal conductivity of glass compared to air or glycerol.

Note for a homogeneous air environment, the calculated temperature change at steady-state is 104 K. This is much larger than the temperature change for the 0% embedded particles in Figure 6(a), showing that the glass substrate has a significant influence on heat dissipation, even when the

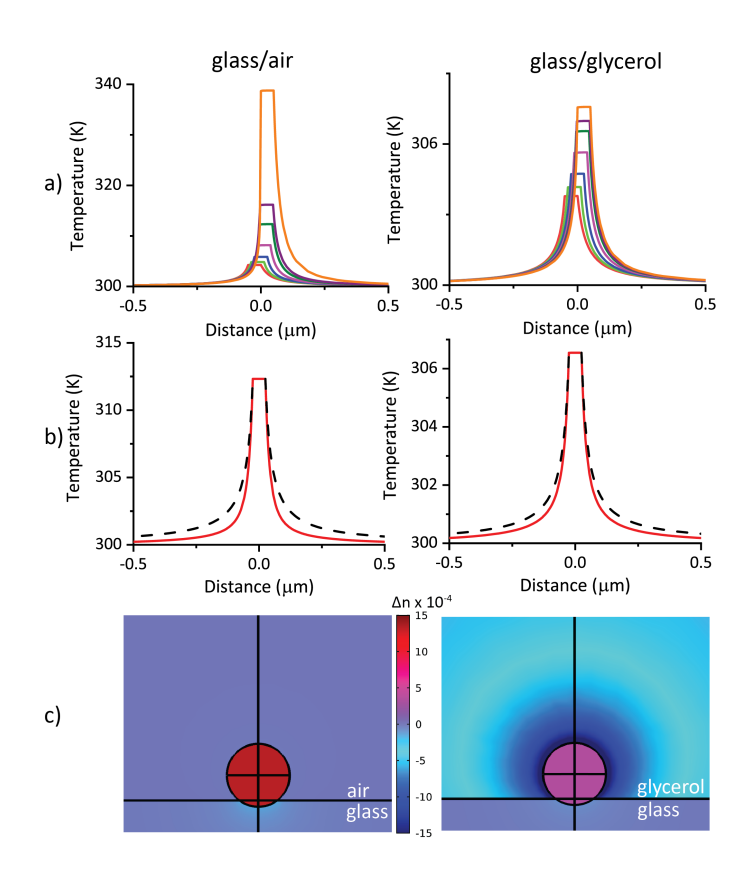


Figure 6: Simulations of the temperature and refractive index profiles at steady-state for a 50 nm gold nanoparticle on a glass surface in air (left) and glycerol (right). (a) Temperature profiles through the center of the particle perpendicular to the interface for different amounts of particle embedding (100%, 75%, 50%, 25%, 10%, 5% and 0%). The glass is at negatives distances. (b) Temperature profile through the center of the particle parallel to the interface for a particle that is 10% embedded in the glass. The dashed lines show the 1/r steady state curve. (c) Plots of the change in refractive index Δn of the system for a 10% embedded particle. Note the different sign of Δn for the gold compared to the surroundings

particles are only just touching the surface. This is attributed to heat transfer through the air to the glass substrate.⁵⁰

There are several points to note from the temperature profiles in Figures 6(a) and 6(b). First, the temperature profiles in the environment at steady-state do not follow 1/r curves for cutlines either perpendicular or parallel to the interface, unlike what was observed for particles in a homogeneous environment. Second, the temperature profiles are not symmetric along the line perpendicular to the interface. The increase in temperature extends further into the material with the higher thermal diffusivity, which is air for the glass/air system, and glass for the glass/glycerol system (see Supporting Information).

To evaluate how the interface affects spatial resolution in PHI microscopy, the temperature changes obtained from the heat transfer simulations were multiplied by the dn/dT for the different materials.^{23, 28} Images for the glass/air and glass/glycerol interfaces for a 10% embedded particle are show in Figure 6(c). For the glass/air interface the refractive index changes are dominated by the gold particle. This is because the values of dn/dT for glass and air are much smaller than the value estimated for gold. In this case the spatial resolution in PHI microscopy experiments will simply be determined by the convolution of the laser point-spread-function and the size of the nanoparticle being interrogated, and there will be no frequency dependence in the images. For the glass/glycerol interface the change in refractive index of the glycerol is comparable to that of gold, so that the temperature change in the glycerol will contribute to the thermal lens. A frequency dependence in the images is now expected. The effect will be similar to that in Figure 4, although the PHI point-spread-function will be slightly reduced because the temperature profile parallel to the interface decays faster than 1/r for substrate supported particles (see Figure 6(b)).

4. Conclusions:

The effect of heat dissipation on the spatial resolution in PHI experiments was investigated experimentally and through finite element simulations. Images recorded for Au nanoparticles with co-focused pump and probe beams show no changes with the timescale of the measurement, which is controlled by the pump beam modulation frequency. This is because for co-focused experiments the PHI signal is only generated when the pump beam is on the nanoparticle being studied, which means that these measurements essentially image nanoparticle absorption. A small change in spatial resolution with timescale was observed for experiments with a widefield pump, where the nanoparticle is continuously heated as the images are formed. However, the spatial extent of the features in the PHI images are much smaller than the thermal diffusion length R_{th} . Heat transfer simulations show that the lack of sensitivity to timescale arises because the nanoparticles rapidly reach a steady-state condition, where heating from optical excitation is balanced by energy dissipation into the environment.³⁶ In this case the temperature profile around the particle is independent of the thermal diffusion length. The steady-state condition is reached for modulation frequencies less than 100 kHz for gold nanoparticles in the normal environments used for PHI experiments. At higher frequencies a narrowing of the PHI point-spread-function is expected, but the effects are small compared to the spatial resolution in typical optical microscopes.

Acknowledgements: The authors acknowledge the support of the National Science Foundation through Award CHE-1902403, and through a DOE SBIR Phase IIb grant (DE-SC0018519). Any opinions, findings, and conclusions or recommendations expressed in this material are those of the authors and do not necessarily reflect the views of the National Science Foundation or the Department of Energy.

Conflicts of Interest:

The authors declare that there are no conflicts of interest for the present work.

Supplementary Information: Supporting information for this paper contains a schematic of the optical system for the PHI experiments, additional PHI images and z-axis scans of the PHI signal, details of the finite element simulations, images of the mesh used in the COMSOL simulations, values for the different parameters, and additional simulation results.

References:

- 1. Boyer, D.; Tamarat, P.; Maali, A.; Lounis, B.; Orrit, M., Photothermal Imaging of Nanometer-Sized Metal Particles among Scatterers. *Science* **2002**, *297*, 1160-1163.
- 2. Berciaud, S.; Cognet, L.; Blab, G. A.; Lounis, B., Photothermal Heterodyne Imaging of Individual Nonfluorescent Nanoclusters and Nanocrystals. *Physical Review Letters* **2004**, *93*, 257402.
- 3. van Dijk, M. A.; Tchebotareva, A. L.; Orrit, M.; Lippitz, M.; Berciaud, S.; Lasne, D.; Cognet, L.; Lounis, B., Absorption and Scattering Microscopy of Single Metal Nanoparticles. *Phys. Chem. Chem. Phys.* **2006**, *8*, 3486-3495.
- 4. Cognet, L.; Berciaud, S.; Lasne, D.; Lounis, B., Photothermal Methods for Single Nonluminescent Nano-Objects. *Analytical Chemistry* **2008**, *80*, 2288-2294.
- 5. Berciaud, S.; Cognet, L.; Lounis, B., Luminescence Decay and the Absorption Cross Section of Individual Single-Walled Carbon Nanotubes. *Physical Review Letters* **2008**, *101*, 077402.
- 6. Jollans, T.; Baaske, M. D.; Orrit, M., Nonfluorescent Optical Probing of Single Molecules and Nanoparticles. *Journal of Physical Chemistry C* **2019**, *123*, 14107-14117.
- 7. Adhikari, S.; Spaeth, P.; Kar, A.; Baaske, M. D.; Khatua, S.; Orrit, M., Photothermal Microscopy: Imaging the Optical Absorption of Single Nanoparticles and Single Molecules. *ACS Nano* **2020**, *14*, 16414-16445.
- 8. Berciaud, S.; Cognet, L.; Tamarat, P.; Lounis, B., Observation of Intrinsic Size Effects in the Optical Response of Individual Gold Nanoparticles. *Nano Letters* **2005**, *5*, 515-518.
- 9. Berciaud, S.; Cognet, L.; Lounis, B., Photothermal Absorption Spectroscopy of Individual Semiconductor Nanocrystals. *Nano Letters* **2005**, *5*, 2160-2163.
- 10. Berciaud, S.; Cognet, L.; Poulin, P.; Weisman, R. B.; Lounis, B., Absorption Spectroscopy of Individual Single-Walled Carbon Nanotubes. *Nano Letters* **2007**, *7*, 1203-1207.
- Lasne, D.; Blab, G. A.; Berciaud, S.; Heine, M.; Groc, L.; Choquet, D.; Cognet, L.; Lounis, B., Single Nanoparticle Photothermal Tracking (Snapt) of 5-Nm Gold Beads in Live Cells. *Biophysical Journal* 2006, 91, 4598-4604.
- 12. Gaiduk, A.; Yorulmaz, M.; Ruijgrok, P. V.; Orrit, M., Room-Temperature Detection of a Single Molecules Absorption by Photothermal Contrast. *Science* **2010**, *330*, 353-356.
- 13. Lasne, D.; Blab, G. A.; De Giorgi, F.; Ichas, F.; Lounis, B.; Cognet, L., Label-Free Optical Imaging of Mitochondria in Live Cells. *Opt. Express* **2007**, *15*, 14184-14193.

- 14. Gaiduk, A.; Yorulmaz, M.; Ishow, E.; Orrit, M., Absorption, Luminescence, and Sizing of Organic Dye Nanoparticles and of Patterns Formed Upon Dewetting. *ChemPhysChem* **2012**, *13*, 946-951.
- 15. Nedosekin, D. A.; Galanzha, E. I.; Ayyadevara, S.; Reis, R. J. S.; Zharov, V. P., Photothermal Confocal Spectromicroscopy of Multiple Cellular Chromophores and Fluorophores. *Biophysical Journal* **2012**, *102*, 672-681.
- 16. He, J. P.; Miyazaki, J.; Wang, N.; Tsurui, H.; Kobayashi, T., Biological Imaging with Nonlinear Photothermal Microscopy Using a Compact Supercontinuum Fiber Laser Source. *Opt. Express* **2015**, *23*, 9762-9771.
- 17. He, J. P.; Wang, N.; Tsurui, H.; Kato, M.; Iida, M.; Kobayashi, T., Noninvasive, Label-Free, Three-Dimensional Imaging of Melanoma with Confocal Photothermal Microscopy: Differentiate Malignant Melanoma from Benign Tumor Tissue. *Scientific Reports* **2016**, *6*, 30209.
- 18. Zhang, D.; Li, C.; Zhang, C.; Slipchenko, M. N.; Eakins, G.; Cheng, J.-X., Depth-Resolved Mid-Infrared Photothermal Imaging of Living Cells and Organisms with Submicrometer Spatial Resolution. *Science Advances* **2016**, *2*, e1600521.
- 19. Li, Z.; Aleshire, K.; Kuno, M.; Hartland, G. V., Super-Resolution Far-Field Infrared Imaging by Photothermal Heterodyne Imaging. *The Journal of Physical Chemistry B* **2017**, *121*, 8838-8846.
- 20. Bai, Y. R.; Zhang, D. L.; Li, C.; Liu, C.; Cheng, J. X., Bond-Selective Imaging of Cells by Mid-Infrared Photothermal Microscopy in High Wavenumber Region. *Journal of Physical Chemistry B* **2017**, *121*, 10249-10255.
- 21. Pavlovetc, I. M.; Podshivaylov, E. A.; Chatterjee, R.; Hartland, G. V.; Frantsuzov, P. A.; Kuno, M., Infrared Photothermal Heterodyne Imaging: Contrast Mechanism and Detection Limits. *Journal of Applied Physics* **2020**, *127*, 165101.
- 22. Berciaud, S.; Lasne, D.; Blab, G. A.; Cognet, L.; Lounis, B., Photothermal Heterodyne Imaging of Individual Metallic Nanoparticles: Theory Versus Experiment. *Physical Review B* **2006**, *73*, 045424.
- 23. Gaiduk, A.; Ruijgrok, P. V.; Yorulmaz, M.; Orrit, M., Detection Limits in Photothermal Microscopy. *Chemical Science* **2010**, *1*, 343-350.

- 24. Selmke, M.; Braun, M.; Cichos, F., Photothermal Single-Particle Microscopy: Detection of a Nanolens. *ACS Nano* **2012**, *6*, 2741-2749.
- 25. Selmke, M.; Braun, M.; Cichos, F., Nano-Lens Diffraction around a Single Heated Nano Particle. *Opt. Express* **2012**, *20*, 8055-8070.
- 26. Bhattacharjee, U.; West, C. A.; Hosseini Jebeli, S. A.; Goldwyn, H. J.; Kong, X.-T.; Hu, Z.; Beutler, E. K.; Chang, W.-S.; Willets, K. A.; Link, S., et al., Active Far-Field Control of the Thermal near-Field Via Plasmon Hybridization. *ACS Nano* **2019**, *13*, 9655-9663.
- 27. Hosseini Jebeli, S. A.; West, C. A.; Lee, S. A.; Goldwyn, H. J.; Bilchak, C. R.; Fakhraai, Z.; Willets, K. A.; Link, S.; Masiello, D. J., Wavelength-Dependent Photothermal Imaging Probes Nanoscale Temperature Differences among Subdiffraction Coupled Plasmonic Nanorods. *Nano Letters* 2021, 21, 5386-5393.
- 28. Goldwyn, H. J.; Link, S.; Masiello, D. J., Resolving Resonance Effects in the Theory of Single Particle Photothermal Imaging. *arXiv*: 2103.01494v2 2021, arXiv: 2103.01494v2.
- 29. Berto, P.; Mohamed, M. S. A.; Rigneault, H.; Baffou, G., Time-Harmonic Optical Heating of Plasmonic Nanoparticles. *Physical Review B* **2014**, *90*, 035439.
- 30. Selmke, M.; Cichos, F., The Physics of the Photothermal Detection of Single Absorbing Nano-Objects: A Review. *arXiv*: 1510.08669v1 **2018**, arXiv:1510.08669.
- 31. Harada, M.; Shibata, M.; Kitamori, T.; Sawada, T., Application of Coaxial Beam Photothermal Microscopy to the Analysis of a Single Biological Cell in Water. *Analytica Chimica Acta* **1995**, *299*, 343-347.
- 32. Dada, O. O.; Feist, P. E.; Dovichi, N. J., Thermal Diffusivity Imaging with the Thermal Lens Microscope. *Appl. Opt.* **2011**, *50*, 6336-6342.
- 33. Heber, A.; Selmke, M.; Cichos, F., Thermal Diffusivity Measured Using a Single Plasmonic Nanoparticle. *Physical Chemistry Chemical Physics* **2015**, *17*, 20868-20872.
- 34. Heber, A.; Selmke, M.; Cichos, F., Thermal Diffusivities Studied by Single-Particle Photothermal Deflection Microscopy. *ACS Photonics* **2017**, *4*, 681-687.
- 35. Zahedian, M.; Lee, Z.; Koh, E. S.; Dragnea, B., Studies of Nanoparticle-Assisted Photoannealing of Polydimethylsiloxane by Time-Harmonic Photothermal Microscopy. *ACS Photonics* **2020**, *7*, 2601-2609.
- 36. Carslaw, H. S.; Jaeger, J. C., *Conduction of Heat in Solids*; Oxford University Press: Oxford 1959.

- 37. Govorov, A. O.; Zhang, W.; Skeini, T.; Richardson, H.; Lee, J.; Kotov, N. A., Gold Nanoparticle Ensembles as Heaters and Actuators: Melting and Collective Plasmon Resonances. *Nanoscale Research Letters* **2006**, *1*, 84-90.
- 38. Keblinski, P.; Cahill, D. G.; Bodapati, A.; Sullivan, C. R.; Taton, T. A., Limits of Localized Heating by Electromagnetically Excited Nanoparticles. *Journal of Applied Physics* **2006**, *100*, 054305.
- 39. Govorov, A. O.; Richardson, H. H., Generating Heat with Metal Nanoparticles. *Nano Today* **2007**, *2*, 30-38.
- 40. Baffou, G.; Quidant, R.; de Abajo, F. J. G., Nanoscale Control of Optical Heating in Complex Plasmonic Systems. *Acs Nano* **2010**, *4*, 709-716.
- 41. Setoura, K.; Okada, Y.; Werner, D.; Hashimoto, S., Observation of Nanoscale Cooling Effects by Substrates and the Surrounding Media for Single Gold Nanoparticles under Cw-Laser Illumination. *ACS Nano* **2013**, *7*, 7874-7885.
- 42. Selmke, M.; Braun, M.; Cichos, F., Gaussian Beam Photothermal Single Particle Microscopy. *J. Opt. Soc. Am. A* **2012**, *29*, 2237-2241.
- 43. Selmke, M.; Cichos, F., Photothermal Single Particle Rutherford Scattering Microscopy. *Physical Review Letters* **2013**, *110*, 103901.
- 44. Selmke, M.; Cichos, F., Photonic Rutherford Scattering: A Classical and Quantum Mechanical Analogy in Ray and Wave Optics. *American Journal of Physics* **2013**, *81*, 405-413.
- 45. Wilson, O. M.; Hu, X. Y.; Cahill, D. G.; Braun, P. V., Colloidal Metal Particles as Probes of Nanoscale Thermal Transport in Fluids. *Physical Review B* **2002**, *66*, 224301.
- 46. Hartland, G. V., Optical Studies of Dynamics in Noble Metal Nanostructures. *Chemical Reviews* **2011**, *111*, 3858-3887.
- 47. Parra-Vasquez, A. N. G.; Oudjedi, L.; Cognet, L.; Lounis, B., Nanoscale Thermotropic Phase Transitions Enhancing Photothermal Microscopy Signals. *Journal of Physical Chemistry Letters* **2012**, *3*, 1400-1403.
- 48. Chang, W.-S.; Link, S., Enhancing the Sensitivity of Single-Particle Photothermal Imaging with Thermotropic Liquid Crystals. *The Journal of Physical Chemistry Letters* **2012**, *3*, 1393-1399.

- 49. Ding, T. N. X.; Hou, L.; van der Meer, H.; Alivisatos, A. P.; Orrit, M., Hundreds-Fold Sensitivity Enhancement of Photothermal Microscopy in near-Critical Xenon. *Journal of Physical Chemistry Letters* **2016**, *7*, 2524-2529.
- 50. Großer, J.; Furstenberg, R.; Kendziora, C. A.; Papantonakis, M. R.; Borchert, J.; Andrew McGill, R., Modeling of the Heat Transfer in Laser-Heated Small Particles on Surfaces. *Int. J. Heat Mass Transf.* **2012**, *55*, 8038-8050.

TOC graphic:

